Hyperspectral reflectance spectra of floating matters derived from HICO observations

Chuanmin Hu

College of Marine Science, University of South Florida, St. Petersburg, Florida, 33701, USA

Correspondence to: Chuanmin Hu (huc@usf.edu)

Abstract

Using data collected by the Hyperspectral Imager for the Coastal Ocean (HICO) on the International Space Station between 2010 – 2014, hyperspectral reflectance of various floating matters in global oceans and lakes are derived for the spectral range of 400 – 800 nm. Specifically, the entire HICO archive of 9,411 scenes is first visually inspected to identify suspicious image slicks. Then, a nearest-neighboring atmospheric correction is used to derive surface reflectance of slick pixels. Finally, a spectral unmixing scheme is used to derive the reflectance spectra of floating matters. Analysis of the spectral shapes of these various floating matters (macroalgae, microalgae, organic particles, whitecaps) through the use of a Spectral Angle Mapper (SAM) index indicates that they can mostly be distinguished from each other without the need of ancillary information. Such reflectance spectra from the consistent 90-m resolution HICO observations are expected to provide spectral endmembers to differentiate and quantify the various floating matters from existing multi-band satellite sensors and future hyperspectral satellite missions such as NASA's Plankton, Aerosol, Cloud, and ocean Ecosystem (PACE) mission and Surface Biology and Geology (SBG) mission.

Keywords: Remote sensing, hyperspectral, HICO, OCI, PACE, SBG, floating matters, *Ulva, Sargassum, Noctiluca, Trichodesmium, Microcystis,* brine shrimp, oil slicks, whitecaps, marine debris.

1. Introduction

Since the debut of the first proof-of-concept Coastal Zone Color Scanner (CZCS, 1978 – 1986), satellite ocean color missions have evolved from the original goal of mapping phytoplankton biomass and primary production to many other applications. Because of improved spectral resolution and instrument sensitivity, mapping various floating matters also becomes possible (IOCCG, 2014). These floating matters range from living to non-living, including *Sargassum* macroalgae, *Ulva* macroalgae, cyanobacterium *Microcystis*, cyanobacterium *Trichodesmium*, dinoflagellate *Noctiluca*, aquatic plants, brine shrimp cysts, oil slicks, pumice rafts, sea snots, marine debris, among others (Qi et al., 2020; Hu et al., 2022).

Currently, mapping floating matters using optical remote sensing requires the detection of a spatial anomaly using the near-infrared (NIR) bands, and then discrimination of the anomaly by comparing its spectral characteristics with known spectra of floating matters (Qi et al., 2020), or by using ancillary information (e.g., in certain regions a spatial anomaly can only be caused by a certain type of floating algae). Spectral discrimination requires the knowledge of

spectral signatures of various floating matters. However, despite scattered laboratory or field measurements of certain types of floating matters, hyperspectral data of these floating matters are mostly unavailable. Although medium-resolution (300-m) sensors such as the Ocean and Land Colour Imager (OLCI) has been used to show spectral variations of floating matters (Qi et al., 2020), the data are not hyperspectral, therefore certain spectral features may have been missed. For example, various pigments (e.g., chlorophyll-*a*, *b*, *c*, Fucoxanthin, Zeaxanthin, phycocyanin, carotenoid, etc.) have been found in natural populations of microalgae (i.e., phytoplankton, Bidigare et al., 1990; Bricaud et al., 2004) and macroalgae (e.g., Bell et al., 2015; Wang et al., 2018). These pigments often have narrow absorption and reflectance features that can be missed by multi-band sensors, therefore requiring more spectral bands or hyperspectral data to perform spectroscopic analysis.

Data collected by the Hyperspectral Imager for the Coastal Ocean (HICO) on the International Space Station may serve for this purpose. HICO has 128 bands covering a spectral range of 353 – 1080 nm. From its entire mission of 2010 – 2014, a total of > 10,000 scenes have been collected at a spatial resolution of about 90 m, each containing about 512 × 2000 pixels. On average, only 6 scenes were collected per day around the globe, mostly over land and coastal waters. Because of its stable calibration (Ibrahim et al., 2018) and relatively high signal-to-noise ratios (Hu et al., 2012), deriving hyperspectral surface reflectance of water targets should be feasible. Indeed, after vicarious calibration and atmospheric correction, hyperspectral reflectance data over water have been generated (Ibrahim et al., 2018) and made available through the NASA OB.DAAC (https://oceancolor.gsfc.nasa.gov). However, these data products are not applicable to image pixels containing floating matters due to their interference with the atmospheric correction scheme.

The primary objective of this paper is to derive HICO-based hyperspectral reflectance of various floating matters. This requires customized atmospheric correction and pixel unmixing to account for the small proportion of floating matters within an image pixel. From such derived spectra, a secondary objective is to analyze whether they can be differentiated spectrally. Similar to the compiled hyperspectral dataset for inherent and apparent optical properties to support future hyperspectral missions such as NASA's Plankton, Aerosol, Cloud, and ocean Ecosystem (PACE) mission (Casey et al., 2020), such a dataset for floating matters is expected to help develop or improve algorithms for the PACE mission as well as for the hyperspectral Surface Biology and Geology mission currently being planned by NASA (Cawse-Nicholson et al., 2021).

2. Data and Methods

HICO Level-1B (calibrated radiance) data were obtained from the NASA Goddard Space Flight Center (https://oceancolor.gsfc.nasa.gov). Of the total collected >10,000 scenes, 9,411 were available through this data portal. They were all downloaded, and the following 4 steps were used to derive spectral reflectance of various floating matters.

Step 1 is to generate quick look Red-Green-Blue (RGB) and False-color RGB (FRGB) images with Rayleigh corrected reflectance (R_{rc}, dimensionless) in three HICO bands using the same methods as in Qi et al. (2020) and in the NOAA OCview online tool (Mikelsons and Wang, 2018). In the FRGB images, a near-infrared (NIR) band is used to represent

77 the green channel, thus making floating matters often appear greenish due to their elevated NIR reflectance. Here, R_{rc}

78 was generated using the NASA software SeaDAS (version 7.5). Mathematically, it is derived as

79 $\qquad R_{rc} = (R_t - R_r)/(t\, t_o\, t_{O2}\, t_{H2O}),$

80 $\qquad R_t = \pi\, L_t^* / F_o \cos(\theta_o),$

81 $\qquad R_r = \pi\, L_r / F_o \cos(\theta_o),$ $\hfill$ (1)

82 where L_t^* is the at-sensor total radiance after vicarious calibration and adjustment of two-way gaseous absorption (e.g.,

83 Ozone), L_r is at-sensor radiance due to Rayleigh scattering, F_o is the extraterrestrial solar irradiance, θ_o is the solar

84 zenith angle, t is the diffuse transmittance from the image pixel to the satellite, t_o is the diffuse transmittance from the

85 sun to the image pixel, t_{O2} and t_{H2O} are the two-way transmittance due to absorption by atmospheric O_2 and H_2O,

86 respectively. For simplicity, the wavelength dependency is omitted here.

87 Step 2 is to determine image slicks through visual inspection of both RGB and FRGB images. Fig. 1a shows an FRGB

88 image captured in the central western Atlantic, where an elongated greenish slick is identified.

89 Step 3 is to derive surface reflectance (R, dimensionless) of the slick pixels (i.e., those containing floating matters)

90 *and* nearby water pixels. While the latter is straightforward because R at each pixel is a standard output of the SeaDAS

91 software, the former is problematic because standard atmospheric correction in SeaDAS fails over floating matters

92 due to their elevated NIR reflectance. Such elevated NIR reflectance violates the atmospheric correction assumptions

93 (i.e., negligible reflectance in the NIR, or fixed relationships between the red and NIR wavelengths) for slick pixels.

94 Therefore, a nearest-neighbor atmospheric correction (Hu et al., 2000) was used to estimate R of the slick pixels.

95 Specifically, from the SeaDAS output of R_{rs}, we have

96 $\qquad R = \pi\, R_{rs} = (R_t - R_r - R_a)/(t\, t_o\, t_{O2}\, t_{H2O}),$ $\hfill$ (2)

97 where R_{rs} is the surface remote sensing reflectance (sr^{-1}), R_a is the at-sensor aerosol reflectance (and reflectance due

98 to aerosol-molecule interactions as well as due to sun glint and whitecaps). The difference between R and R_{rc} in Eqs.

99 (2) and (1), respectively, is the removal of R_a in (2). Estimation of R_a at each pixel represents the "core" of any

100 atmospheric correction scheme. The SeaDAS estimation of R_a is valid over water pixels, but not valid over the slick

101 pixels. Therefore, R_a over water pixels was used as a surrogate to represent R_a over the nearby slick pixels, from which

102 R over slick pixels was derived. This is why such an approach is called "nearest-neighbor" atmospheric correction

103 (Hu et al., 2000). In this context, the slick pixel is called "target", and the nearby water pixel is called "reference".

104 Their surface reflectance are called R^T and R^R, respectively. Fig. 1b shows examples of R^T and R^R.

105

106

107

108

109

110

111
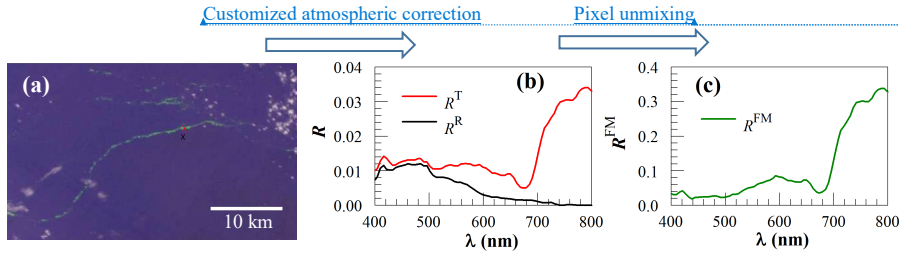
Formatted: Font: 10 pt

Formatted: Font: 10 pt

112

113

114

115

116

117 **Figure 1. Demonstration of how surface reflectance of floating matter (R^{FM}) is derived. (a) FRGB image on 1 July 2012**

118 **showing several greenish image slicks in the Amazon River plume. The image covers a region of about 40 km × 24 km, with**

119 **the "Target" (6.65914ºN, 51.2395ºW) and "Reference" (6.64847ºN, 51.2411ºW) pixels marked with a red "×" and a black**

120 **"×", respectively. (b) Their corresponding R^T and R^R, with the latter derived from SeaDAS and the former derived from a**

121 **nearest-neighbor atmospheric correction. (c) R^{FM} derived from R^T and R^R using Eq. (4), with χ being estimated to be 10%.**

122

123 The final step, Step 4, is to perform spectral unmixing of R^T. This is because floating matters often cover only a small

124 portion a pixel (Hu, 2021a). In this step, the derived R^T from Step 3 is assumed to be a linear mixture of two

125 endmembers: floating matter (R^{FM}) and water (R^W):

126 $$R^T = \chi R^{FM} + (1 - \chi)R^W = \chi R^{FM} + (1 - \chi)R^R \qquad (3)$$

127 Here, χ is the subpixel portion of floating matter which can vary between 0.0% and 100%, R^W is assumed to be R^R.

128 Then, the final product, R^{FM}, is derived as

129 $$R^{FM} = R^R + (R^T - R^R)/\chi \qquad (4)$$

130 In the right-hand side of Eq. (4), the only unknown is χ. In practice, assuming R^{FM} at 750 nm ≈ 0.3 as revealed by

131 independent measurements of floating macroalgae (Hu, L. et al., 2017; Wang et al., 2018), χ is estimated through

132 linear unmixing as

133 $$\chi = [R^T(754) - R^R(754)]/[0.3 - R^R(754)] \qquad (5)$$

134 Here, with $R^T(754)$ varying between $R^R(754)$ and 0.3, χ ranges between 0.0% and 100%. Plugging this mixing ratio

135 into Eq. (4) will derive R^{FM}. Fig. 1c shows the example of how R^{FM} is derived from R^T and R^R of Fig. 1b once they are

136 known from Step 3, with χ being estimated to be 10%.

137 Once R^{FM} is derived, a spectral angle mapper index (SAM, Kruse et al., 1993) was used to determine whether different

138 floating matters were spectrally different. SAM was used because it is based on spectral shape only. SAM is the angle

139 between two spectral vectors, defined as (Kruse et al., 1993):

140 $$\text{SAM (degrees)} = \cos^{-1}[(\sum x_i y_i) / (\sqrt{\sum x_i^2} \sqrt{\sum y_i^2})]. \qquad (6)$$

141 Here, x and y represent two spectral vectors with the ith band from 1 to N. An SAM of 0º indicates identical spectral
142 shapes between x and y regardless of their difference in magnitudes, while an SAM of 90º indicates completely
143 different spectral shapes. An SAM of < 5º indicates that the two spectra are very similar (Garaba and Dierssen, 2018).

144 **3. Results: HICO reflectance spectra of floating matters**

145 The approach above was applied to the visually identified image slicks to derive $R^{FM}(\lambda)$. These include: 1) *Sargassum*
146 *fluitans/natans* in the Atlantic (including the Caribbean Sea and Gulf of Mexico), 2) *Ulva prolifera* in the western
147 Yellow Sea (near Qingdao, China), 3) *Kelp* in South Atlantic, 4) *Trichodesmium* around Australia, in the Gulf of
148 Mexico and Persian Gulf, in the South Atlantic Bight, Bay of Bengal, near Hawaii and Pagan Island (middle Pacific),
149 5) Cyanobacteria of *Microcystis* in Taihu Lake, Lake Woods, and Lake of Victoria, 6) Red *Noctiluca scintillas* (*RNS*)
150 in the East China Sea, and coastal waters off Japan, 7) Brine shrimp cysts in the Great Salt Lake, 8) Oil slicks in the
151 Gulf of Mexico, 9) Whitecaps (foam) in the Arabian Sea, Caspian Sea, and Bohai Sea, 10) Ice in Lake Baykal, 11)
152 some unknown algae features. For convenience, they are grouped into 4 figures: Fig. 2 for macroalgae (*Sargassum*,
153 *Ulva*, and kelp), Fig. 3 for microalgae (*Trichodesmium*, *Microcystis*, red *Noctiluca scintillas* or *RNS*), Fig. 4 for organic
154 particles and ocean/lake bubbles, and Fig. 5 for unknown algae scums.

155
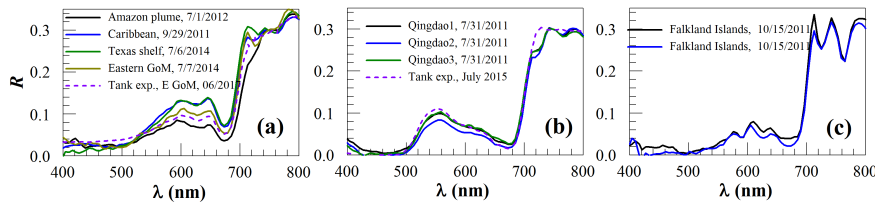
156 **Figure 2: Surface reflectance (*R*, dimensionless) of macroalgae: (a) pelagic *Sargassum fluitains/natans*, (b) *Ulva prolifera*, (c)**
157 **kelp. The dashed lines in (a) and (b) denote *R* from water tank experiments of Wang et al. (2018) and Hu, L. et al. (2017),**
158 **respectively.**

159

160
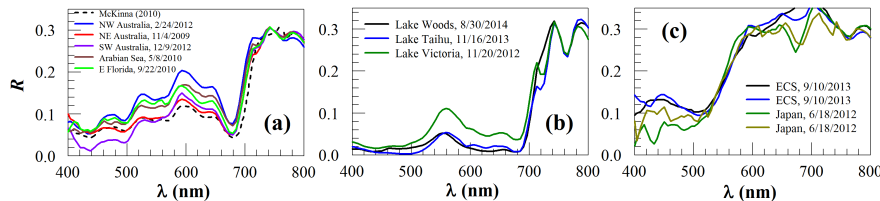
161
162 **Figure 3. Surface reflectance (*R*, dimensionless) of floating scums of microalgae: (a) *Trichodesmium*, (b) *Microcystis*, (c)**
163 **red *Noctiluca* near Yangtze River of the East China Sea and in Sagami Bay of Japan. The dashed line in (a) denote field**
164 **measured *R* by McKinna (2010).**

167

168

169
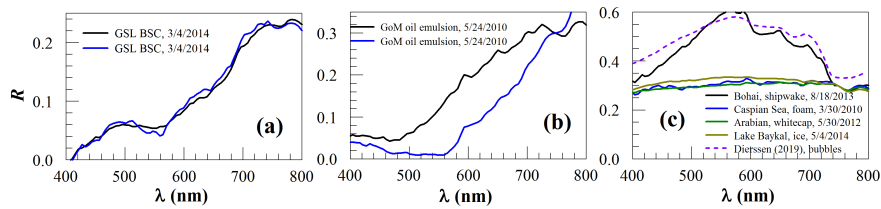
Figure 4: Surface reflectance (*R*, dimensionless) of various floating materials: (a) Brine shrimp cysts in the Great Salt Lake (GSL), (b) emulsified oil from the Deepwater Horizon oil spill, and (c) shipwake, seafoam, whitecap and ice. The dashed line in (c) denotes submersed bubbles measured by Dierssen (2019), which is similar to the shipwake spectrum. Note the similarity among other spectra.

174

185
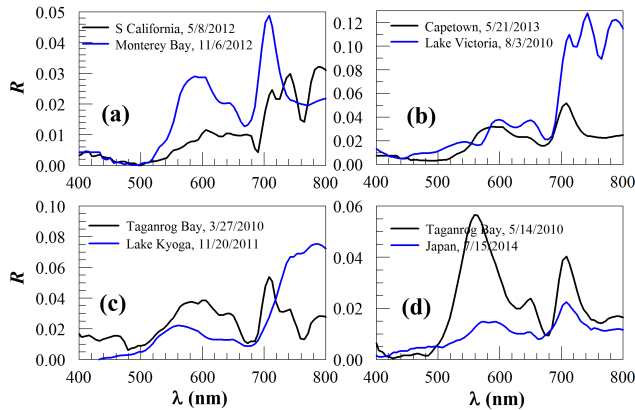
Figure 5: Surface reflectance (*R*, dimensionless) of known and unknown algae scums. (a) Blooms off southern California and in Monterey Bay that are thought to be *Lingulodinium polyedrum* (Cetinic, 2009) and *Akashiwo sanguinea* (Jessup et al., 2009), respectively. (b) Blooms of unknown types of algae off Cape Town (South Africa) and in Lake Victoria, both likely to be dinoflagellates. Note the different spectra shape of the Lake Victoria bloom as compared with the cyanobacterial bloom in the same lake (Fig. 3b). (c) Blooms of unknown types of algae in Taganrog Bay and Lake Kyoga. (d). Blooms of unknown types of algae in Taganrog Bay (note the difference from Fig. 5c) and in Japan coastal waters.

Of all spectra presented in Figs. 2 – 4, one common feature for all floating macroalgae and microalgae (except red *Noctiluca*) is the red-edge reflectance (i.e., the sharp increase from about 670 nm to the NIR wavelengths). Such a common feature is due to both chlorophyll-*a* absorption around 670 nm and high reflectance in the red and NIR wavelengths due to macroalgae mats or microalgae scums (Kazemipour et al., 2011; Launeau et al., 2018). The lack of such a red-edge feature in some of the red *Noctiluca* reflectance spectra (Fig. 3c) is possibly due to the lack of chlorophyll-*a* pigment because red *Noctiluca* is heterotrophic (i.e., it does not contain pigments unless it feeds on other algae). Other than the common red-edge reflectance, the contrasting spectral shapes of the various types of floating macroalgae and microalgae are due to their different pigment compositions (see below). In contrast, the non-leaving floating matters do not show red-edge reflectance or other pigment-induced spectral features in the visible wavelengths (Fig. 4). In Fig. 5, in addition to pigment absorption, high scattering due to high concentrations of algae particles together with sharp increases of water absorption from the red to the NIR wavelengths lead to the local reflectance peak around 700 nm (Fig. 5) and, depending on the particle concentrations, the peak wavelength may be slightly shifted, for example from 700 to 710 nm.

4. Discussion

4.1. Uncertainties in the derived RFM

There are several assumptions used in the nearest-neighbor atmospheric correction and spectral unmixing (Eq. 4). Violations of these assumptions will cause errors in the derived R^{FM} spectra. For example, if the atmosphere over the floating matter pixel is different from over the nearby water, the nearest-neighbor atmospheric correction may not be applicable. In practice, however, because the target and reference pixels are very close (< 1 km), such a violation is unlikely. In Step 4, the water within the FM-containing pixel is assumed to be the same as the nearby water. Because of the close proximity of the two pixels, this assumption should be valid for most cases unless the FM-containing pixel is at an ocean front where different water masses converge. The departure of $R^{FM}(754)$ from the assumed 0.3 will also lead to errors in the estimated χ (and therefore R^{FM}). However, as long as R^W (i.e., R^R) in Eqs. (4) & (5) is $<< R^{FM}$, the shape of R^{FM} is still retained, although the magnitude departs from the "truth" in proportional to the departure of $R^{FM}(754)$ from 0.3. Indeed, the condition of $R^W << R^{FM}$ can be satisfied for $\lambda > 600$ nm for most floating matters unless the water is extremely turbid. Even for turbid waters, for certain floating matters where R^{FM} is elevated at $\lambda > 530$ nm (e.g., red *Noctiluca*, brine shrimp cysts, ice), the shape of the derived R^{FM} should still be valid for $\lambda > 530$ nm. Indeed, when R^W is $<< R^{FM}$, even a simple subtraction of R_{rc} or TOA radiance between the target pixel and reference pixel, as demonstrated in Gower et al. (2006), may retain the spectral shapes of floating matters.

Another uncertainty source can come from the assumption of linear mixing between floating matters and water (Eq. (3)). For macroalgae, the linear mixing up to the reflectance saturation level has been shown in laboratory experiments (Hu. L et al., 2017; Wang et al., 2018). As long as the macroalgae stay on the very surface of water (as opposed to be submerged under the surface), this assumption should be valid not just for macroalgae but for all floating matters. For the same reason, if certain portions of kelp are submerged in water, large uncertainties may result from the linear

227 unmixing scheme. Under high-wind conditions, the strong mixing may result in submerged algae (especially for

228 microalgae), thus violating the linear mixing rule. However, the cases presented in Figs. 2 - 5 were selected very

229 carefully to avoid high wind speed (> 5 m s^{-1}, where wind speed was obtained from the National Centers for

230 Environmental Prediction). Therefore, such mixing induced uncertainties are unlikely.

231 Additional uncertainties may come from the HICO radiometric calibration, which affects R_t and all derivative products.

232 Through the use of the Marine Optical Buoy (MOBY) and other clear-water sites, HICO has been calibrated

233 vicariously (Ibrahim et al., 2018), which resulted in significant improvements in the retrieved R_{rs} over water as

234 compared with data without vicarious calibration. However, after the vicarious calibration, while the spectral shape

235 of R_{rc} over water appears correct, the shape of ΔR_{rc} over land appears to be biased low at $\lambda > 800$ nm. Without vicarious

236 calibration, the opposite is observed. This is possibly due to the non-linear effects in the detector response to incoming

237 light, and currently there appears no reliable way to address this issue (A. Ibrahim, personal comm.). Similarly,

238 calibration for $\lambda < 450$ nm may be subject to larger errors than for λ between 450 and 800 nm. Therefore, R^{FM} in the

239 range of 800 – 900 nm is omitted here, and interpretation of 400 – 450 also requires more caution. Similarly, the

240 spectral wiggling between 700 and 800 nm (e.g., Fig. 3b) appears to come from residual errors in correcting water

241 vapor absorption and oxygen absorption in the atmosphere. Therefore, although the spectral wiggling does not affect

242 the overall shape of the red-edge reflectance, it may not be used for algorithm development to discriminate floating

243 matter types.

244 Indeed, with all these possible sources of uncertainties, such HICO-derived R^{FM} can still be used for spectral

245 discrimination of different floating matters without ambiguity, as shown below.

4.2. Implications for spectral discrimination

247 Spectral discrimination can be performed through either visual inspection or the use of certain type of similarity index

248 (e.g., SAM, Eq. 6). Here, results of the SAM analysis are presented in Table 1, followed by descriptions of visual

249 inspection to interpret the spectral similarity or difference. Because nearly all floating algae show typical red edge

250 reflectance, discrimination of different algae type is focused on wavelengths < 670 nm. To discriminate floating algae

251 from non-living floating matters (e.g., marine debris), on the other hand, the inclusion of 670 nm is critical.

252 Furthermore, because HICO data are noisy for wavelengths < 450 nm, the SAM calculation was restricted to 450 –

253 670 nm from most R^{FM} spectra of Figs. 2 – 4.

254 Table 1 shows the SAM results for three types of macroalgae (*Sargassum*, *Ulva*, kelp), three types of microalgae

255 (*Trichodesmium*, *Microcystic*, red *Nocticula scintillas* or *RNS*), and one type of organic matter (brine shrimp cysts or

256 *BSC*). **Here, unless noted, *Sargassum* refers to *Sargassum fluitans/natans* (dominant pelagic type in the Atlantic**

257 **ocean) and *Ulva* refers to *Ulva prolifera* (dominant pelagic type in the Yellow Sea).** For the same floating matter,

258 if field-based R^{FM} is available, then it is used as the reference, otherwise the mean HICO-derived R^{FM} is used as the

259 reference. For SAM between different floating matters, all HCIO-derived R^{FM} from both types are used (e.g., 4

260 *Sargassum* R^{FM} of Fig. 2a and 3 *Ulva* R^{FM} of Fig. 2b are used to calculate 12 SAM values), with their mean and

261 standard deviations listed in Table 1.

Table 1. Spectral Angle Mapper values (degrees) between different floating matters for the spectral range of 450 – 670 nm, derived from the HICO-derived and field-measured spectra shown in Figs. 2-4. An SAM of 0° indicates identical spectral shape, while an SAM of 90° indicates completely different spectral shape. *Sarg*: *Sargassum fluitans/natans*; *Ulva: Ulva prolifera*; *Tricho*: *Trichodesmium*; *Micro*: *Microcystis*; *RNS*: red *Noctiluca scintillas*; *BSC*: brine shrimp cysts. Because all floating algae show similar red-edge reflectance with a reflectance trough around 670 nm, the exclusion of wavelengths of > 670 nm is to reduce the similarity among different types of floating algae.

Sarg	4.5±1.6						
Ulva	27.2±2.5	2.9±0.5					
Kelp	13.7±1.8	32.5±1.3	2.7±0.4				
Tricho	15.4±4.6	25.1±2.0	23.1±3.2	2.8±2.0			
Micro	32.9±7.5	16.8±5.6	39.0±7.7	28.8±5.1	4.6±2.5		
RNS	9.9±2.4	31.4±2.8	16.7±3.0	17.2±2.1	34.7±6.7	1.8±0.7	
BSC	20.7±0.9	39.3±2.4	27.0±3.1	21.2±1.6	40.9±5.5	14.5±3.1	1.1±0.0
	Sarg	*Ulva*	*Kelp*	*Tricho*	*Micro*	*RNS*	*BSC*

For each type of floating matter, HICO-derived R^{FM} is very similar to either field-measured R^{FM} or to their mean R^{FM}, with SAM < 4.6°. In contrast, SAM between different floating matters is always > 9.9°. These results suggest that, if these floating matters represent all that can be found in natural waters, they can be differentiated through spectroscopy analysis without any other ancillary information (e.g., knowledge of local oceanography or dominant floating algae type). This is despite the possible uncertainties in their reflectance magnitude, as discussed above. In the natural environments, however, there may be other types of floating algae whose spectral shapes may be similar to *Sargassum fluitans/natans* (e.g., *Sargassum honeria* in the East China Sea *or* other brown algae) or *Ulva prolifera* (e.g., other green algae). Therefore, some form of ancillary information in addition to spectroscopy is still required in order to differentiate floating algae type.

The results from the SAM table can also be explained through visual inspection and interpretation of the spectral shapes, as discussed below.

From Fig. 2, it is clear that although the three types of macroalgae all share the same red-edge reflectance in the NIR, they have different spectral shapes in the visible wavelengths. Unlike the *Ulva* reflectance with a local peak around 560 nm, the spectral shapes of *Sargassum* reflectance resemble those of typical brown algae where the local reflectance trough around 625 nm is induced by chlorophyll-*c* absorption and the low reflectance below ~520 nm is due to carotenoid pigment absorption. These characteristics make it easy to distinguish *Sargassum* from *Ulva* (SAM > 27°, Table 1). On the other hand, it appears more difficult to spectrally discriminate *Sargassum* from kelp because they

304   both have reference peaks around 600 – 645 nm, and because they also share a common reflectance trough around

305   625 nm. However, considering *Sargassum* is moving in the ocean while kelp is fixed in location, they can be separated

306   using sequential images. Even from a single image, when most visible wavelengths are used, *Sargassum* and kelp can

307   still be spectrally discriminated (SAM > 13°, Table 1). Within the group of *Sargassum* spectra (Fig. 2a), there is some

308   variability in the magnitude between 560 – 700 nm. It is unclear what caused such variability, although it could be

309   due to changes in carbon to chlorophyll ratio in *Sargassum* of different environment, as observed from kelp (Bell et

310   al., 2015). Such a variability, however, would not impact the spectral discrimination of *Sargassum* against other

311   floating matters, as SAM between *Sargassum* spectra is < 5°, much lower than between *Sargassum* and any other

312   floating matters (Table 1).

313   Similar to the macroalgae, the microalgae scums also show elevated NIR reflectance (Fig. 3), and their spectral shapes

314   in the visible make them straightforward to distinguish from each other (SAM > 17°), and also straightforward to

315   distinguish from macroalgae (SAM > 9.9°). One exception may be the cyanobacterial scums (blue-green algae blooms)

316   (Fig. 3b) as they show reflectance peak around 550 nm, similar to *Ulva* (Fig. 2b). However, reflectance around 550

317   nm is nearly symmetric for cyanobacterial scums, but asymmetric for *Ulva*. There is also a local reflectance trough

318   around 625 nm for cyanobacterial scums due to absorption of phycocyanin, but such a trough is lacking in the *Ulva*

319   spectra. Such characteristic makes it possible to differentiate between the two even without *a priori* knowledge of the

320   ocean or lake environment, as the SAM between the two groups is ~16.8° (Table 1). What's interesting is that within

321   each class, either *Trichodesmium* or *Microcystis*, although the spectral shape is nearly identical from different spectra

322   (SAM < 5°), there is substantial variability in the magnitude in the visible wavelengths, which might be due to changes

323   in their carbon to chlorophyll ratios (Behrenfeld et al., 2005). Furthermore, the spectral wiggling features between 450

324   and 660 nm in Fig. 3a are due to *Trichodesmium*-specific pigments such as phycourobilin, phycoerythrobilin, and

325   phycocyanin that absorb light strongly at 495, 550, and 625 nm, respectively (Navarro Rodriguez, 1998). These

326   features are unique to *Trichodesmium* scums, which make it straightforward to develop classification algorithms once

327   certain spectral bands are available to capture these features (e.g., Hu et al., 2010).

328   Of all microalgae scums of Fig. 3, the spectral shapes of red *Noctiluca* (Fig. 3c) appear different from all others, but

329   they show the same characteristics as reported from the limited field measurements (Van Mol et al., 2007): a sharp,

330   featureless increase from ~520 nm to ~600 nm. This unique spectral shape makes *RNS* different from all other floating

331   matters (SAM > 9.9°, Table 1). The difference within this group is that the spectra from Sagami Bay off Japan show

332   reflectance troughs around 670 nm. Because red *Noctiluca* is known to feed on other algae, it is speculated that the

333   670-nm trough is due to chlorophyll pigments of the consumed algae. Once more hyperspectral data are available in

334   the future to test this hypothesis using field data, this characteristic may be used to study how red *Noctiluca* interacts

335   with other algae. On the other hand, once more hyperspectral data are available in the future, it is also possible to test

336   whether other algae (e.g., *Mesodinium rubrum*, Dierssen et al., 2015), once forming surface scums, have similar

337   spectral shapes as those of red *Noctiluca*.

338   The non-algae floating matters in Fig. 4 show spectral characteristics different from both macroalgae and microalgae,

339   for example they lack the typical red-edge reflectance of vegetation, and lack of typical spectral variations in the

340   visible wavelengths due to pigment absorption. Within this group, the organic matters of BSC (Fig. 4a) and emulsified

341   oil (Fig. 4b) show some degrees of similarity as they also have monotonic reflectance increases from a wavelength

342   between 500 – 560 nm to at least 740 nm. The difference between them is that BSC reflectance starts to increase

343   always at ~560 nm with an inflection wavelength ~640 nm, while reflectance of oil emulsions start to increase at

344   variable wavelengths without any inflection between 560 – 740 nm. Indeed, the infection at ~640 nm appears to be a

345   common feature between BSC slicks and coral spawn slicks (Yamano et al., 2020). In contrast, depending on the oil

346   emulsion state, oil emulsion may have different spectral characteristics (Lu et al., 2019), suggesting that there is no

347   fixed "endmember" spectra for oil spills.

348   The inorganic "particles" (i.e., water bubbles, ice) also have distinctive spectral shapes. The examples in Fig. 4c

349   indicate that submersed bubbles from shipwakes are similar in spectral shapes, but all others are nearly identical in

350   their lack of any spectral features. Rather, foams, whitecaps, and ice all show flat reflectance spectral shapes between

351   400 – 800 nm that are consistent with *in situ* measurements of foams (Dierssen, 2019). The lack of spectral features

352   is similar to marine debris (Garaba and Dierssen, 2020). Such a similarity will make detection of marine debris very

353   difficult, especially around ocean fronts because these are where surface materials tend to aggregate and foams also

354   tend to form.

355   In addition to the spectra of Figs. 2-4 that can be well recognized, HICO also showed reflectance spectra that are

356   difficult to discriminate from spectroscopy alone, as shown in Fig. 5. Without a known reflectance library, one can

357   only speculate what algae type could be responsible for the algae scum spectra from some ancillary information in the

358   literature. For example, the often reported blooms of *Lingulodinium polyedrum* and *Akashiwo sanguinea* in coastal

359   waters off southern California and in Monterey Bay, respectively, may show spectral shapes of Fig. 5a when they are

360   heavily concentrated in surface waters. Inference may also be made for other cases once similar ancillary information

361   is available. Even when such information is absent, one can still rule out some possibilities simply based on the spectral

362   shapes. For example, the reflectance spectrum in Fig. 5b from Lake Victoria cannot be from cyanobacteria that has

363   been often reported in this lake (Fig. 3b), but it is most likely from a dinoflagellate bloom, as blooms of other algae

364   types have also been reported in this lake (Haande et al., 2011). Likewise, the different spectra from the same Taganrog

365   Bay in Figs. 5c & 5d suggest different algae type. Clearly, although cyanobacterial blooms have been reported in

366   many lakes, without spectral diagnosis one cannot simply jump to the conclusion that a freshwater bloom is caused

367   by a certain type of cyanobacterium.

368   **4.3. Implications for current and future satellite missions**

369   Because HICO is a pathfinder sensor that collected only a limited number of scenes, not all reported floating matters

370   have been captured. For example, no HICO scene appears to have captured pumice rafts, *Sargassum horneri*, sea snots,

371   or marine debris. Therefore, the spectral reflectance dataset presented here is incomplete. The use of data from other

372   similar pathfinders, for example the DLR Earth Sensing Imaging Spectrometer (DESIS) on the ISS (235 bands from

373   400 – 1000 nm, 30-m resolution, 2018 – present) and the PRecursore IperSpettrale della Missione Applicativa

374   (PRISMA, 237 bands from 400 – 2505 nm, 30-m resolution, 2019 – present), may complement the spectral data using

Deleted: pure

Deleted:

Deleted: 0

378 the same approach (e.g., sea snot reflectance spectra, Hu et al., 2022). Even at its present form, given the large variety

379 of floating matters presented here, the spectral data may lead to several implications for current and future satellite

380 missions.

381 First, although all current multi-band sensors can detect floating matters through their elevated NIR reflectance (Qi et

382 al., 2020), the Sentinel-3 Ocean and Land Colour Imager (OLCI) appears to be the best to differentiate spectral shapes

383 in the visible wavelengths because of its 21 spectral bands between 400 and 1,020 nm, especially because of its 620-

384 nm that can be used to differentiate whether an algae scum appears greenish or brownish, thus providing extra

385 information to discriminate algae type in the absence of hyperspectral data.

386 Second, for the same reason, although only 4 bands (blue, green, red, NIR) are available on the PlanetScope (DOVE)

387 constellation, the recent SuperDOVE constellation is equipped with 4 additional bands with one centered at 610 nm,

388 thus may significantly enhance the capacity of the current high-resolution sensors (~ 3-4 m or 30 m) in differentiating

389 greenish and brownish algae types.

390 Finally, the Ocean Color Instrument (OCI) on NASA's PACE mission, to be launched in 2023, will be the first of its

391 kind to map global oceans with hyperspectral capacity (5 nm resolution between 340 – 890 nm, plus 7 discrete bands

392 from 940 to 2260 nm) with a nominal resolution of 1 km. Unlike HICO, OCI will cover global oceans and lakes every

393 1-2 days, thus providing unprecedented opportunities to detect, differentiate, and quantify various types of floating

394 matters. The spectral reflectance data, derived from one sensor (HICO) with a stable calibration, may serve as a

395 consistent dataset to help select the optimal bands towards future applications once PACE data becomes available, for

396 example, through the use of SAM matrix as demonstrated in Table 1. Likewise, the SBG mission currently being

397 planned by NASA is expected to have hyperspectral capacity between 380 and 2500 nm with a nominal resolution of

398 30 m (Cawse-Nicholson et al., 2021); such a mission will provide unprecedented opportunity to map various floating

399 matters on a global scale where the hyperspectral dataset developed here can help develop algorithms before its launch.

400 **5. Conclusion**

401 Through customized atmospheric correction and spectral unmixing, hyperspectral reflectance in the visible and NIR

402 wavelengths of various floating matters have been derived from HICO measurements over global oceans and lakes.

403 The reflectance dataset shows distinguishable spectral shapes between floating algae (macroalgae and microalgae)

404 and non-algae floating matters (*Sargassum fluitans/natans*, *Ulva prolifera*, *kelp*, *Microcystis*, *Trichodesmium*, red

405 *Noctiluca scintillas*, brine shrimp cysts), and also distinguishable spectral shapes in the visible wavelengths between

406 different floating algae types. While the approach may be extended to other pathfinder missions to complement the

407 findings here, the spectral reflectance dataset is expected to help select optimal bands for future hyperspectral satellite

408 missions to differentiate and quantify the various floating matters in global oceans and lakes.

Deleted: if there is room to allow for more than

Deleted: such as those

Deleted: s

Deleted: a 5th band may be placed around 620 nm. Then, with the existing bands in the blue, green, red, and NIR region, such a 5-band sensor

Deleted: , 4-band sensors

Deleted: ¶

Deleted: ¶

Formatted: Font: 10 pt

Formatted: Normal

Formatted: Font: Italic

Formatted: Font: 10 pt

Data Availability

All HICO data used in this analysis are available at the NASA Ocean Biology Distributed Active Archive Center (OB.DAAC, https://oceancolor.gsfc.nasa.gov). The data processing software (SeaDAS) can be obtained from the same source, at https://seadas.gsfc.nasa.gov. The derived HICO spectra in digital data form, as shown in the above figures, are available on-line from the Ecological Spectral Information System (EcoSIS) (http://ecosis.org, doi: 10.21232/74LvC3Kr) (Hu, 2021b).

Acknowledgements

This work was supported by the U.S. NASA (NNX17AF57G, 80NSSC21K0422). I thank NASA and the U.S. Naval Research Lab for providing HICO data, thank Lachlan McKinna for providing field-measured reflectance of *Trichodesmium*, and thank Heidi Dierssen for providing field-measured reflectance of whitecaps. Dr. Patrick Launeau and Dr. Qianquo Xing provided useful comments to improve the presentation of this work, whose efforts are appreciated.

References

[1] Behrenfeld, M. J., E. Boss, D. A. Siegel, and D. M. Shea (2005). Carbon-based ocean productivity and phytoplankton physiology from space. Global Biogeochemical Cycles, 19, GB1006, doi:10.1029/2004GB002299.

[2] Bell, T. W., K. C. Cavanaugh, and D. A. Siegel (2015). Remote monitoring of giant kelp biomass and physiological condition: An evaluation of the potential for the Hyperspectral Infrared Imager (HyspIRI) mission. *Remote Sens. Environ.*, 167:218-228.

[3] Bidigare, R. R., M. E. Ondrusek, J. H. Morrow, and D. A. Kiefer (1990). In-vivo absorption properties of algal pigments. In Orlando'90, 16– 20 April. 290–302.

[4] Bricaud, A., Claustre, H., Ras, J., Oubelkheir, K. (2004). Natural variability of phyto- planktonic absorption in oceanic waters: influence of the size structure of algal populations. Journal of Geophysical Research 109. http://dx.doi.org/10.1029/ 2004JC002419.

[5] Casey, K. A., C. S. Rousseaux, W. W. Gregg, et al. (2020). A global compilation of in situ aquatic high spectral resolution inherent and apparent optical property data for remote sensing applications. Earth Syst. Sci. Data, 12:1123-1139. https://doi.org/10.5194/essd-12-1123-2020.

[6] Cawse-Nicholson, K. P. A. Townsend, D. Schimel, et al. (2021). NASA's surface biology and geology designated observable: A perspective on surface imaging algorithms. *Remote Sens. Environ.*, 257, 112349, https://doi.org/10.1016/j.rse.2021.112349

[7] Dierssen, H., G. B. McManus, A. Chlus, D. Qiu, B-C. Gao, and S. Lin (2015). Space station image captures a red tide ciliate bloom at high spectral and spatial resolution, 112(48), 14,783-14,787, https://www.pnas.org/cgi/doi/10.1073/pnas.1512538112

451   [8]   Dierssen, H. (2019). Hyperspectral Measurements, Parameterizations, and Atmospheric Correction of
452   Whitecaps and Foam From Visible to Shortwave Infrared for Ocean Color Remote Sensing. Front. Earth Sci.
453   7:14. doi: 10.3389/feart.2019.00014.
454   [9]   Garaba, S. P., and H. M. Dierssen (2018). An airborne remote sensing case study of synthetic hydrocarbon
455   detection using short-wave infrared absorption features identified from marine-harvested macro- and
456   microplastics. *Remote Sens. Environ.* 2018, *205*, 224–235.
457   [10]   Garaba, S. P., and H. M. Dierssen (2020). Hyperspectral ultraviolet to shortwave infrared characteristics of
458   marine-harvested, washed-ashore and virgin plastics. Earth Syst. Sci. Data, 12, 77–86, 2020
459   https://doi.org/10.5194/essd-12-77-2020.
460   [11]   Gower, J., Hu, C., Borstad, G., King, S. (2006). Ocean color satellites show extensive lines of floating
461   Sargassum in the Gulf of Mexico. *IEEE Transactions on Geoscience and Remote Sensing*, 44, 3619-3625.
462   [12]   Haande, S., Rohrlack, T., Semyalo, R.P., Brettum, P., Edvardsen, B., Lyche-Solheim, A., Sørensen, K., &
463   Larsson, P. (2011). Phytoplankton dynamics and cyanobacterial dominance in Murchison Bay of Lake Victoria
464   (Uganda) in relation to environmental conditions. *Limnologica-Ecology Management of Inland Waters, 41*, 20-
465   29.
466   [13]   Hu, C., Carder, K. L., and Muller-Karger, F. E. (2000), Atmospheric correction of SeaWiFS imagery over
467   turbid coastal waters: a practical method, Remote Sens. Environ. 74:195-206.
468   [14]   Hu, C., J. Cannizzaro, K. L.Carder, F. E. Muller-Karger, and R. Hardy (2010). Remote
469   detection of Trichodesmium blooms in optically complex coastal waters: Examples with
470   MODIS full-spectral data. Remote Sens. Environ., 114:2048-2058.
471   [15]   Hu, C., L. Feng, Z. Lee, C. O. Davis, A. Mannino, C. R. McClain, and B. A. Franz (2012). Dynamic range and
472   sensitivity requirements of satellite ocean color sensors: learning from the past. Appl. Opt., 51:6045-6062.
473   [16]   Hu, L., Hu, C., & Ming-Xia, H. (2017). Remote estimation of biomass of Ulva prolifera macroalgae in the
474   Yellow Sea. *Remote Sensing of Environment, 192*, 217-227.
475   [17]   Hu, C. (2021a). Remote detection of marine debris using satellite observations in the visible and near infrared
476   spectral range: Challenges and potentials. *Remote Sens. Environ*., 259,
477   112414, https://doi.org/10.1016/j.rse.2021.112414
478   [18]   Hu, C. (2021b). Floating matter reflectance from HICO. Data set. Available on-line [http://ecosis.org] from the
479   Ecological Spectral Information System (EcoSIS). 10.21232/74LvC3Kr.
480   [19]   Hu, C., L. Qi, Y. Xie, S. Zhang, and B. B. Barnes (2022). Spectral characteristics of sea snot
481   reflectance observed from satellites: Implications for remote sensing of marine debris.
482   Remote Sens., Environ, 269, 112842, https://doi.org/10.1016/j.rse.2021.112842
483   [20]   Ibrahim, A., B. A. Franz, Z. Ahmad, R. Healy, K. Knobelspiesse, B-C. Gao, C. Proctor, and P-W. Zhai (2018).
484   Atmospheric correction for hyperspectral ocean color retrieval with application to the Hyperspectral Imager
485   for the Coastal Ocean (HICO). *Remote Sensing of Environment*, 204:60-75,
486   http://dx.doi.org/10.1016/j.rse.2017.10.041.

488   [21]   IOCCG (2014). Phytoplankton Functional Types from Space. Sathyendranath, S. (ed.), Reports of the
489   International Ocean-Colour Coordinating Group, No. 15, IOCCG, Dartmouth, Canada.

490   [22]   Kazemipour, F., V. Méléder, and P. Launeau (2011). Optical properties of microphytobenthic biofilms
491   (MPBOM): Biomass retrieval implication. Journal of Quantitative Spectroscopy and Radiative Transfer.
492   112:131-142, https://doi.org/10.1016/j.jqsrt.2010.08.029

493   [23]   Kruse, F, A., A.B. Lefkoff, J.W. Boardman, K.B. Heidebrecht, A.T. Shapiro, P.J. Barloon, A.F.H. Goetz
494   (1993). The spectral image processing system (SIPS)—interactive visualization and analysis of imaging
495   spectrometer data. *Remote Sensing Environ.*, 44:145-163.

496   [24]   Launeau, P., V. Méléder, C. Verpoorter, et al. (2018). Microphytobenthos Biomass and Diversity Mapping at
497   Different Spatial Scales with a Hyperspectral Optical Model. Remote Sensing, 10, 716;
498   doi:10.3390/rs10050716.

499   [25]   Lu, Y., Shi, J., Wen, Y., Hu, C., Zhou, Y., Sun, S., Zhang, M., Mao, Z., & Liu, Y. (2019). Optical
500   interpretation of oil emulsions in the ocean – Part I: Laboratory measurements and proof-of-concept with
501   AVIRIS observations. *Remote Sensing of Environment, 230*, 111183.
502   https://doi.org/10.1016/j.rse.2019.05.002.

503   [26]   McKinna, L.I.W. (2015). Three decades of ocean-color remote-sensing Trichodesmium spp. in the World's
504   oceans: A review. *Progress in Oceanography, 131*, 177-199.

505   [27]   Mikelsons, M., and M. Wang (2018). Interactive online maps make satellite ocean data ac- cessible. Eos 99.
506   https://doi.org/10.1029/2018EO096563.

507   [28]   Navarro Rodriguez, A.J. (1998). Optical properties of photosynthetic pigments and abundance of the
508   cyanobacterium Trichodesmium in the eastern Caribbean Basin. Ph.D. Thesis. University of Puerto Rico,
509   Mayaguez (Puerto Rico), Source DAI-B 59/08, p. 3944, Feb 1999, 125 pp.

510   [29]   Qi, L., C. Hu, K. MIkelsons, M. Wang, V. Lance, S. Sun, B. B. Barnes, J. Zhao, and D. V. der Zande (2020).
511   In search of floating algae and other organisms in global oceans and lakes. Remote Sens. Environ., 239,
512   111659, https://doi.org/10.1016/j.rse.2020.111659.

513   [30]   Van Mol, B., Ruddick, K., Astoreca, R., Park, Y., & Nechad, B. (2007). Optical detection of a Noctiluca
514   scintillans bloom. *EARSeL eProceedings, 6*, 130-137.

515   [31]   Wang, M., Hu, C., Cannizzaro, J., English, D., Han, X., Naar, D., et al. (2018). Remote sensing of Sargassum
516   biomass, nutrients, and pigments. Geophysical Research Letters, 45.https://doi.org/10.1029/2018GL078858

517   [32]   Yamano, H., A. Sakuma, and S. Harii (2020). Coral-spawn slicks: Reflectance spectra and detection using
518   optical satellite data. Remote Sens. Environ., 251, https://doi.org/10.1016/j.rse.2020.112058.

519